RAA 2016 Vol. **16** No. **11**, 177 (6pp) doi: 10.1088/1674–4527/16/11/177
© 2016 National Astronomical Observatories, CAS and IOP Publishing Ltd.
http://www.raa-journal.org *http://iopscience.iop.org/raa*

***R**esearch in*
***A**stronomy and*
***A**strophysics*

The Energetics of White-light Flares Observed by *SDO*/HMI and *RHESSI*

Neng-Yi Huang[1], Yan Xu[1,2] and Haimin Wang[1,2]

[1] Center for Solar-Terrestrial Research, New Jersey Institute of Technology, Newark, NJ 07102-1982, USA; *nh72@njit.edu*

[2] Big Bear Solar Observatory, Big Bear City, CA 92314, USA

Received 2016 April 30; accepted 2016 August 15

Abstract White-light (WL) flares have been observed and studied for more than a century since their first discovery. However, some fundamental physics behind the brilliant emission remains highly controversial. One of the important facts in addressing the flare energetics is the spatio-temporal correlation between the WL emission and the hard X-ray (HXR) radiation, presumably suggesting that energetic electrons are the energy sources. In this study, we present a statistical analysis of 25 strong flares ($\geq$M5) observed simultaneously by the Helioseismic and Magnetic Imager (HMI), on board the *Solar Dynamics Observatory* (*SDO*), and the *Reuven Ramaty High Energy Solar Spectroscopic Imager* (*RHESSI*). Among these events, WL emission was detected by *SDO*/HMI in 13 flares, associated with HXR emission. To quantitatively describe the strength of WL emission, equivalent area (EA) is defined as the integrated contrast enhancement over the entire flaring area. Our results show that the EA is inversely proportional to the HXR power-law index, indicating that stronger WL emission tends to be associated with a larger population of high energy electrons. However, no obvious correlation is found between WL emission and flux of non-thermal electrons at 50 keV. For the other group of 13 flares without detectable WL emission, the HXR spectra are softer (larger power-law index) than those flares with WL emission, especially for the X-class flares in this group.

Key words: Sun: flares — Sun: white-light — Sun: hard X-ray

1 INTRODUCTION

White-light (WL) flares are characterized by a sudden emission in the visible continuum against the bright photospheric background. In the literature, they are always associated with strong X-ray bursts and, therefore, are classified in the top group of *GOES* classification (Neidig & Cliver 1983a). However, this empirical statistic is subject to limitations in observing techniques; for instance, the spatio-temporal resolution and dynamic range of detectors. With the development of both space-based and ground-based instruments, WL flares have become increasingly resolvable. Zirin (1988) and Neidig (1989) predicted that WL emission may exist in all flares at different levels, but were thought to be only detectable in strong flares. Matthews et al. (2003) surveyed observations of flares in G-band from *Yohkoh* and found a flare in a *GOES* class down to C7.8 with a brightening signal. Hudson et al. (2006) investigated flares observed by the *Transition Region and Coronal Explorer* (*TRACE*). By removing the UV line contaminations, the authors detected WL emission of a flare in a *GOES* class of C1.6. Jess et al. (2008) studied a C2.0 flare that occurred on 2007 August 24 and was observed with the high-resolution ground-based Swedish Solar Telescope (SST), and reported that the contrast of WL emission at its peak time above the quiescent flux was as high as 300%, which appears, however, in a very small area. Wang et al. (2008) surveyed flares observed by *Hinode* and suggested that M1 class is the lower limit for a flare with detectable WL emission observed by *Hinode*.

Since the first discovery of WL flares by Carrington in 1859, tremendous efforts have been made in solving the puzzle of their energetics. It is widely accepted that the initial energy release comes from the corona by magnetic reconnection, from which a huge amount of electrons are accelerated to near relativistic speeds and part of them penetrate to the lower atmosphere spiraling along magnetic field lines (Najita & Orrall 1970; Hudson 1972). However, the formation height and mechanisms of the WL emission remain highly controversial. Several models have been proposed to address these questions. For instance, the direct heating model indicates that the continuum emission is generated by precipitating electrons via collision and ionization in the lower atmosphere (Brown 1971). However, considering the density and short collision range of the upper atmosphere, the electron energy for direct heating should be critically high: 350 keV electrons can only precipitate to the minimum temperature region (Aboudarham & Henoux 1986). Emslie (1978) calculated the relation between required energies of electrons to penetrate to certain

layers and the corresponding densities. As a result, to heat the photosphere ($\tau_{5000} = 1$) the initial energy should be at least a few MeV. Moreover, to generate a WL flare, the total population of electrons to be accelerated in the corona would be too high. Nevertheless, the hypothesis of direct heating is not necessarily the only mechanism. A good alternative explanation is that the electrons stop, release their energies and then heat the lower layer to power the continuum emission by back warming (Machado et al. 1989; Metcalf et al. 1990; Ding 2003).

All the flare models assume that the WL emission is generated by accelerated electrons (Hudson et al. 1992; Fletcher et al. 2007). A direct diagnosis of the electron beams is hard X-ray (HXR) bremsstrahlung radiation. The associations between WL and HXR during flares were proposed by Rust & Hegwer (1975), and confirmed by observations from both spatial and temporal perspectives (e.g. Neidig et al. 1993a; Xu et al. 2004; Hudson et al. 2006). Therefore, coordinated analysis of WL and HXR can reveal the mechanism of how these high-energy electrons should generate bursts of emissions. Battaglia & Kontar (2011) compared extreme ultraviolet (EUV), WL and HXR emission of a limb flare using data from *SDO*/HMI, *SDO*/AIA and the *Reuven Ramaty High Energy Solar Spectroscopic Imager* (*RHESSI*). They found that the EUV emission comes from higher layers (3 Mm from the photosphere) where low energy electrons ($\sim$ 12 keV) deposit their energies. The HXR of 35–100 keV is suggested to be in lower layers in a range of 1.7 Mm to 0.8 Mm and the WL is located a little higher at 1.5 Mm. Martínez Oliveros et al. (2012) related WL with HXR in a similar energy range of 30–80 keV. However, they found the formation heights were rather lower for both WL and HXR at 195 km and 305 km, respectively. Cheng et al. (2015) further confirmed the temporal correlation between WL and HXR emission (26–50 keV) using *SDO* and *Fermi* data, respectively. Hao et al. (2012) studied an M6.3 flare close to the disk center. Their results show a clear Balmer jump and classify this flare as a type I flare (Fang & Ding 1995) with a direct link to electron precipitation.

Motivated by the above case studies, we attempt to relate the quantitative characteristics of WL and HXR emission **statistically**. Besides the total energy carried by accelerated electrons, the distribution of electrons as a function of energy is very important and a key parameter for numerical simulations. By solving the radiative hydrodynamic equations, the atmosphere's response to the precipitating electron beams can be simulated. The original idea was developed for stellar flare emission; therefore, this kind of simulation is simplified to deal with one dimensional configurations (along the direction of flare loops). The input parameters can be assumed or derived from HXR observations. Previous studies have matched the simulated results with the observed emission at a certain level (e.g. Allred et al. 2005; Cheng et al. 2010; Rubio da Costa et al. 2016). Usually, HXR emissions are formed from two components, thermal and non-thermal emission. Non-thermal emission always has a power-law spectrum, which can be described as one or more linear functions in a log-log plot. The slope of such a linear function, also known as a power-law index, is the key parameter in determining the contribution of high energy electrons to the entire HXR emission. To quantitatively denote the WL emission strength, we followed the work of Wang et al. (2008). For each WL flare, they integrated the contrast over the areas of WL flare kernels and defined this quantity as equivalent area (EA), which describes the strength and extent of WL emissions. In this paper, we present the investigation of a series of WL flares. Comparing and correlating WL and HXR emissions, we try to answer whether direct heating or back warming dominates in powering WL flares.

2 OBSERVATIONS AND DATA REDUCTION

Solar Dynamics Observatory (*SDO*; Pesnell et al. (2012)) has been monitoring the Sun since its first light in 2010 and it is operating with three major instruments–Atmospheric Imaging Assembly (AIA), EUV Variability Experiment (EVE), and Helioseismic and Magnetic Imager (HMI). Among those three, HMI provides full disk maps of visible intensity and vector magnetograms. The intensity maps are obtained by taking six sampling points across the Fe I absorption line 6173.3 Å estimating the Doppler shift, linewidth and line depth, then "reconstructing" the continuum intensity (Schou et al. 2012). The effective cadence of the visible continuum images is 45 s and the angular resolution is around $1''$. *RHESSI* (Lin et al. 2002) was launched in 2002 to explore HXR emissions during solar flares. It is sensitive to an energy range from 3 keV to 17 MeV with various energy resolutions and angular resolutions. The image cadence is usually 4 s, as determined from the period of a full cycle of modulation. In this study, we use *SDO*/HMI intensity images to retrieve the WL flare signals and *RHESSI* HXR data for imaging and spectroscopic analysis.

Our targets are flares with WL emission observed by the HMI WL channel and have coverage by *RHESSI*. Although it has been predicted theoretically and confirmed observationally that the WL emission is a common feature and is not only found in the most violent events, it is still generally accepted that the stronger flares are more likely to be associated with detectable WL enhancement. The reason for this is that detection of WL flares depends on the capabilities of instruments that are used, for instance the resolution and dynamic range. Neidig & Cliver (1983b) found that WL emission can be found only in X-class flares. Wang et al. (2008) extended the lower limit to M-class by studying *Hinode* observations. Using an even larger telescope, the 1-m SST, Jess et al. (2008) found strong WL emission in a C-class flare.

According to the resolution ability of HMI, we set a threshold of M5.0 to select events. In addition, to minimize the projection effect, near limb events ($\geq 50^\circ$) are excluded. Moreover, there are gaps in the *RHESSI* observations, such as satellite night and the South Atlantic

Table 1 Properties of WL Flares

Date	Time	*GOES*	AR#	Location	EA	HXR Spectral Index
2011.02.15	01:43	X2.2	11158	S21W12	1.45	5.30
2011.07.30	02:04	M9.3	11158	N16E32	5.55	4.84
2011.09.06	22:08	X2.1	11283	N16W15	6.31	2.88
2011.09.08	15:32	M6.7	11283	N14W41	0.95	2.79
2012.07.04	09:47	M5.3	11515	S16W15	1.42	3.45
2012.07.05	11:39	M6.1	11515	S17W30	1.20	2.99
2013.11.10	05:07	X1.1	11890	S13W13	2.34	3.98
2014.01.07	10:07	M7.2	11944	S13E13	2.52	3.65
2014.03.29	17:35	X1.0	12017	N10W32	3.20	2.67
2014.10.22	14:02	X1.6	12192	S14E13	0.87	4.46
2014.10.24	21:07	X3.1	12192	S12W31	0.71	6.25
2015.03.10	03:19	M5.1	12297	S15E39	0.83	2.99
2015.03.11	16:11	X2.1	12297	S17E22	1.15	4.33

Table 2 Properties of Flares without WL Emission

Date	Time	*GOES*	AR#	Location	Spectral Index
2011.02.13	17:28	M6.6	11158	S19E01	5.05
2011.03.09	23:10	X1.5	11166	N10W11	5.91
2011.09.25	04:31	M7.4	11302	N12E45	4.25
2012.03.09	3:22	M6.3	11429	N17W01	5.17
2012.05.10	04:11	M5.7	11467	N10E20	3.84
2012.07.12	16:28	X1.4	11520	S20W03	7.61
2014.01.01	18:40	M9.9	11936	S16W45	9.40
2014.04.18	12:50	M7.3	12036	S15W35	2.77
2014.10.22	01:16	M8.7	12192	S13E21	4.02
2014.10.25	16:55	X1.0	12192	S12W31	7.73
2014.12.04	18:05	M6.1	12222	S20W34	5.84
2014.12.18	21:58	M6.9	12242	S18W26	4.07

Anomaly (SAA). Therefore, we need to eliminate events which were not covered by *RHESSI*. In practice, we first select all events covered by *RHESSI* which occurred close to the disk center. During the period from March 2010 to June 2015, 25 flares satisfied the criteria including flares from *GOES* class of M5.1 to X3.1. Among these events, we observed that the WL signals were present not only in the strongest X-class, but also in some of the M-class flares. Moreover, some X class flares do not have detectable WL enhancement signal. Therefore, we split the events into two categories, with and without WL emission, as shown in Tables 1 and 2.

For each event, we obtained a full-disk image sequence observed by HMI about 10 min prior to the HXR flux peak lasting at least 15 minutes. Then, we zoomed in to the flare region with a small FOV including the entire flare sources identified by HXR images. All of the images were then aligned spatially using the first frame as a reference.

Figure 1 shows an example of the X1.0 flare that was acquired on 2014 March 29. The left panel presents an image taken at 17:41:46 UT, which is before the flare and used as the reference frame for alignment. In order to show the WL emission clearly, difference images are constructed by subtracting each image by the reference frame. This process requires a normalization of the image sequence. To do that, a quiet Sun area was selected, indicated by the white box, and the averaged intensity within this area was defined as the background I_b. Then, the normalized images were obtained and the contrast defined by Contrast $= \frac{I-I_b}{I_b}$ was retrieved. The middle panel of Figure 1 shows an image taken during the peak of the flare. A very weak brightening can be seen around the center but it is not significant. In the difference image, shown in the right panel, two elongated flare sources appear as outlined by red contours. To quantitatively describe the WL emission, we defined the EA following Wang et al. (2008). First, we calculate the standard deviation in the reference area, then the threshold was set as three times the standard deviations in this region to obtain the areas of WL sources. Second, we calculate the EA by integrating the contrast enhancement over the entire flaring area (A), such that EA $= \oint_A$ Contrast $d(A)$. As an example, the EA for the 2014–03–29 event is 3.20 arcsec^2. The results of all WL events are listed in Table 1.

For events without detectable WL emission, the flare peak times are defined as the maxima in 25–50 keV HXR emission. HXR spectra during the peak times are then constructed using the default setups of the *RHESSI* GUI with pileup correction because all the events are stronger than M5.0. The spectral fitting involves two models, the variable thermal (vth) and the broken power law (bpow), in which the former represents the thermal HXR component usually in low energy ranges, and the latter represents the non-thermal component. Our interest is in the non-thermal component, representing the high energy part which is usually correlated with the HXR footpoint and WL emissions. The representative parameter of the non-thermal component is the power-law index, which is the absolute value of the slope of the fitted line in log-log space. In principle, the power-law index is inversely correlated with the population of high energy electrons. In other words, a higher power-law index indicates a softer spectrum with relatively less high energy electrons but a lower power-law index represents a harder spectrum with relatively more high energy electrons. Figure 2 shows a sample spectrum of the 2014–03–29 event. The power-law index for this event is

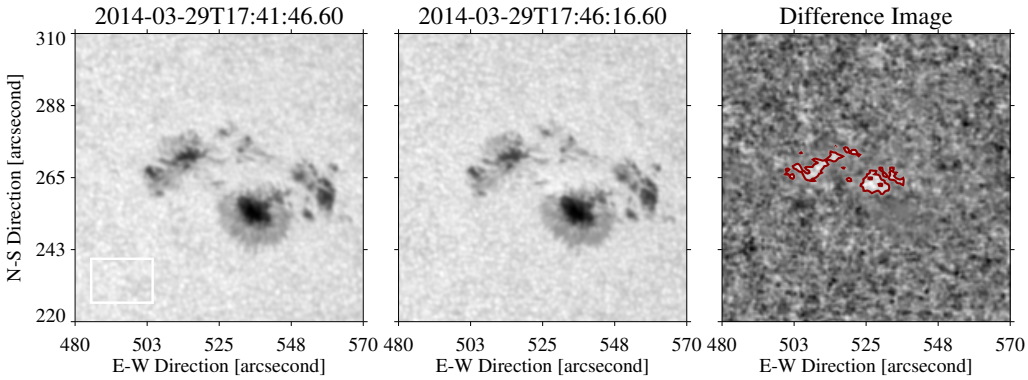

Fig. 1 Image processing steps of an example event, an X1.0 flare on 2014 March 29. *Left panel*: the pre-flare image of the active region, where the region in the white box was selected as the background. *Middle panel*: the flare peak image taken 5 min prior to the WL flare peak. *Right panel*: the difference image of the flare peak subtracting the pre-flare image, where the WL flare ribbons are shown in red contours. The total number of flaring pixels is 124 and the EA is 3.20 arcsec^2.

2.67. We carried out the spectral analysis and obtained the power-law indices for all the 25 events and listed the results in Tables 1 and 2.

3 RESULTS AND DISCUSSION

Among the 25 events we selected, 13 are accompanied by WL flare signals, and the other 12 are not. Figure 3 shows the scatter plot of WL EA vs. HXR power-law index. The red dots represent the X-class flares and the green dots indicate the M-class flares. In principle, we see a correlation between the EA and power-law index. The solid line delineates the trend for all the events and the dotted line delineates the trend for X-class flares only. According to the trend for X-class flares, the **negative correlation** between WL strength and HXR power-law index is more significant. The comparison of EA for WL flares and HXR power-law index shows that flares with smaller HXR indices tend to have larger EAs. On the other hand, for all the M-class flares with WL emission shown in this study, we notice that the HXR spectra are rather hard, with spectral indices smaller than 4. We suspect that other M-class flares with relatively higher power-law index do not have detectable WL emission and are excluded from the analysis. Therefore, this selection effect is one of the reasons why the negative correlation between power-law index and EA is not obvious for M-class flares. As we mentioned in the Introduction section, the power-law index effectively correlates with the population of high-energy electrons. Therefore, the negative correlation between EA and power-law index indicates that the high-energy electrons play a significant role in generating the WL flares, especially the strong (X-class) flares. This result is in favor of the direct-heating model, which requires electrons to have high energy to penetrate down to the lower atmosphere and deposit their energy by collision.

In addition to analyzing multiple events, the temporal variations of WL emissions and HXR power-law indices are retrieved and compared. Figure 4 shows the time evolutions of WL and HXR emission fluxes and HXR power-law index during a sample flare on 2014–03–29. The thick solid curve traces the light curve of WL emission, the dotted curve shows the power-law index evolving as a function of time, and the red and green curves plot the time pro-

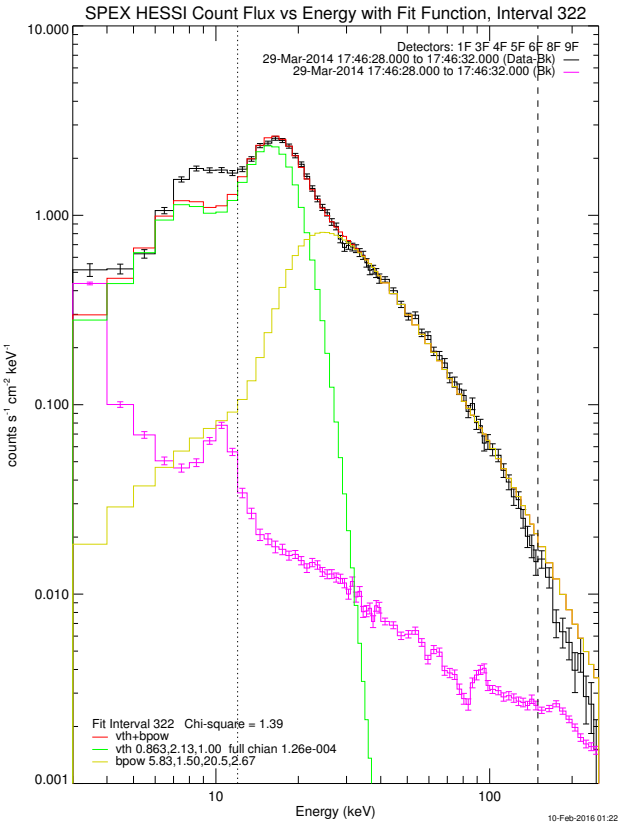

Fig. 2 Fitting of the peak spectrum of the flare on 2014 March 29 using two components of a variable thermal and non-thermal broken power law. The *black curve* is the spectral data after subtracting the background (*pink*). The modeled thermal and non-thermal components, and the overall spectrum, are plotted in *green*, *yellow* and *red*, respectively.

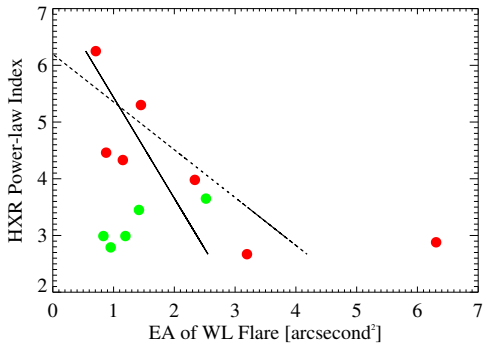

Fig. 3 Plot of EA of WL flare source vs. HXR power-law index. The *solid line* shows the trend from linear fitting for all events. A negative correlation is obviously seen (the lower the power-law index, the larger the EA of WL). The *red dots* represent the X-class flares and the *green dots* indicate the M-class flares. The *dashed line* delineates the trend for X-class flares only.

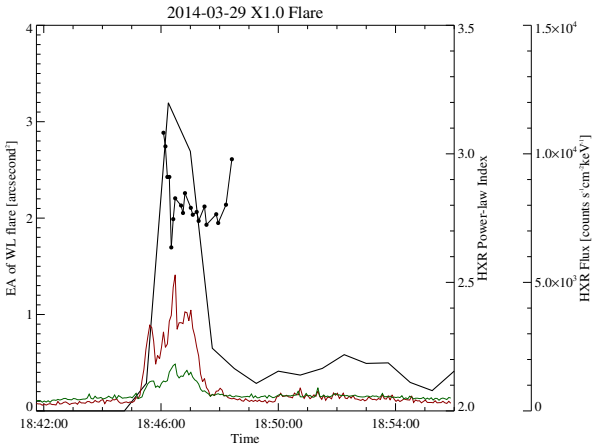

Fig. 4 Time evolutions of WL EA, HXR energy flux and HXR power-law index during the flare on 2014 March 29. The *red* and *green curves* indicate the fluxes of HXR in energy ranges of 50–100 keV and 100–250 keV, respectively. The *thick black curve* shows the temporal variation of WL emission and the *curve with black dots* represents the power-law index evolving as a function of time. As expected, a good correlation between the WL and HXR emission is shown. More importantly, we see a negative temporal correlation between WL emission and HXR power-law index.

files of HXR fluxes in energy ranges of 50–100 keV and 100–250 keV respectively. We see that the WL and HXR fluxes are temporally correlated as expected, and there is a negative correlation between the WL emission and the power-law index, which is typical for all the WL flares in our list.

Furthermore, we looked for the correlation between WL intensities and HXR fluxes for those WL flares. Figure 5 is the scatter plot of WL EAs and HXR peak fluxes at 50 keV. The red dots represent the X-class flares and the green dots indicate the M-class flares. The correlation between EA and HXR flux is not as clear based on the events in our study. Our result is consistent with

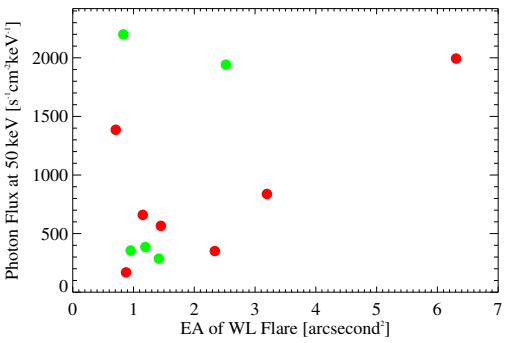

Fig. 5 The scatter plot of WL EAs and HXR peak fluxes at 50 keV. The *red dots* represent the X-class flares and the *green dots* indicate the M-class flares.

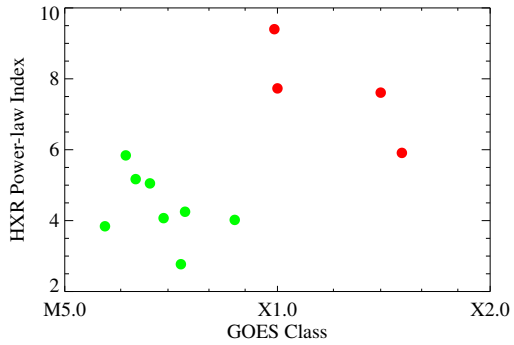

Fig. 6 Plot of *GOES* class and HXR power-law index of non-WL flares. For the X-class flares without obvious WL enhancement, the peak spectra show considerably high HXR power-law indices, but all of the power-law indices for M-class flares are smaller than 6.

Fletcher et al. (2007), in which HXR power above 20 keV and 50 keV was compared with the WL power. Our result suggests that the distribution of high-energy non-thermal electrons is more important, and the electrons with higher energy were more closely related to the generation of WL flares. However, using a larger data set and different method for detecting WL, Kuhar et al. (2016) found a positive correlation between WL emissions and HXR fluxes at 30 keV. Moreover, their result shows no clear correlation between the WL emission and HXR spectral indices, which is also different from our result. The discrepancy is mainly due to the method of measuring the EA of WL emission. For each flare, Kuhar et al. (2016) integrated all the excess WL flux automatically within a certain level of HXR contour. In our study, we manually set thresholds for the WL flare kernels which can be identified visually. Therefore, only the intense flare cores are included in our analysis. According to Neidig et al. (1993b); Xu et al. (2006); Isobe et al. (2007); Xu et al. (2012), the WL flare kernels consist of bright inner cores and relatively weaker halos, corresponding to the direct heating by electrons and the back-warming emission, respectively. The intensity of halo structure is not a monotonically-increasing function of electron energy. Therefore, the relationship between HXR

spectral index and WL intensity is altered for halos. By concentrating on the core emission, we exclude the contamination of halos and other uncertainties introduced by the misalignment among frames in a time sequence.

The HXR power-law indices and the WL EA of the other 12 non-WL flares are plotted in Figure 6. Again, the green and red colors are used for M-class and X-class flares, respectively. It is clear that two distinct groups can be identified for M- and X-class flares. For the X-class flares without detectable WL enhancement, we see that all of the four events have relatively higher power-law indices (>6), which implies that they have less high-energy electrons. This result is consistent with the result of WL flares discussed above. However, for M-class non-WL flares, their power-law indices can be small, indicating the spectra are as hard as the WL flares.

In summary, we surveyed disk-center events above a *GOES* class of M5.0 after *SDO* was launched and covered by *RHESSI*, and 25 were found. We calculated the EA to quantitatively describe the strength of WL emission, as well as the power-law index of HXR to represent the population of high-energy non-thermal electrons which have higher penetrating capability. Comparing the EA and power-law index, we found a negative correlation between them. This result suggests that the high-energy electrons play an important role in flare heating, especially in producing WL emission of strong flares. On the other hand, our result for M-class flares, especially those without WL emission, confirms that the power-law index is not the only or most important parameter to determine WL emission. Considering the complexity of WL and HXR emission, our results in this study are preliminary and can be improved by carrying out more comprehensive analysis. For instance, the $hmi.Ic\_45s$ data from *SDO*/HMI are not real continuum data but reconstructed by intensity data at six spectral points, which can introduce uncertainties in intensity measurements. For future analysis, more precise results can be obtained by including filtergrams without any reconstruction and using higher spatio-temporal resolutions.

Acknowledgements We would like to thank the referee for valuable comments and suggestions. Obtaining the excellent data would not have been possible without the help of the *SDO* and *RHESSI* teams. This work is supported by NSF grants AGS-1539791, AGS-1250374, AGS-1408703 and AGS-1348513.

References

Aboudarham, J., & Henoux, J. C. 1986, Advances in Space Research, 6, 131
Allred, J. C., Hawley, S. L., Abbett, W. P., & Carlsson, M. 2005, ApJ, 630, 573
Battaglia, M., & Kontar, E. P. 2011, A&A, 533, L2
Brown, J. C. 1971, Sol. Phys., 18, 489
Cheng, J. X., Ding, M. D., & Carlsson, M. 2010, ApJ, 711, 185
Cheng, X., Hao, Q., Ding, M. D., et al. 2015, ApJ, 809, 46
Ding, M. D. 2003, Journal of Korean Astronomical Society, 36, S49
Emslie, A. G. 1978, ApJ, 224, 241
Fang, C., & Ding, M. D. 1995, A&AS, 110, 99
Fletcher, L., Hannah, I. G., Hudson, H. S., & Metcalf, T. R. 2007, ApJ, 656, 1187
Hao, Q., Guo, Y., Dai, Y., et al. 2012, A&A, 544, L17
Hudson, H. S. 1972, Sol. Phys., 24, 414
Hudson, H. S., Acton, L. W., Hirayama, T., & Uchida, Y. 1992, PASJ, 44, L77
Hudson, H. S., Wolfson, C. J., & Metcalf, T. R. 2006, Sol. Phys., 234, 79
Isobe, H., Kubo, M., Minoshima, T., et al. 2007, PASJ, 59, S807
Jess, D. B., Mathioudakis, M., Crockett, P. J., & Keenan, F. P. 2008, ApJ, 688, L119
Kuhar, M., Krucker, S., Martínez Oliveros, J. C., et al. 2016, ApJ, 816, 6
Lin, R. P., Dennis, B. R., Hurford, G. J., et al. 2002, Sol. Phys., 210, 3
Machado, M. E., Emslie, A. G., & Avrett, E. H. 1989, Sol. Phys., 124, 303
Martínez Oliveros, J.-C., Hudson, H. S., Hurford, G. J., et al. 2012, ApJ, 753, L26
Matthews, S. A., van Driel-Gesztelyi, L., Hudson, H. S., & Nitta, N. V. 2003, A&A, 409, 1107
Metcalf, T. R., Canfield, R. C., & Saba, J. L. R. 1990, ApJ, 365, 391
Najita, K., & Orrall, F. Q. 1970, Sol. Phys., 15, 176
Neidig, D. F. 1989, Sol. Phys., 121, 261
Neidig, D. F., & Cliver, E. W. 1983a, NASA STI/Recon Technical Report N, 84, 24521
Neidig, D. F., & Cliver, E. W. 1983b, Sol. Phys., 88, 275
Neidig, D. F., Kiplinger, A. L., Cohl, H. S., & Wiborg, P. H. 1993a, ApJ, 406, 306
Neidig, D. F., Wiborg, P. H., & Gilliam, L. B. 1993b, Sol. Phys., 144, 169
Pesnell, W. D., Thompson, B. J., & Chamberlin, P. C. 2012, Sol. Phys., 275, 3
Rubio da Costa, F., Kleint, L., Petrosian, V., Liu, W., & Allred, J. C. 2016, ApJ, 827, 38
Rust, D. M., & Hegwer, F. 1975, Sol. Phys., 40, 141
Schou, J., Scherrer, P. H., Bush, R. I., et al. 2012, Sol. Phys., 275, 229
Wang, H., Jing, J., Tan, C., Wiegelmann, T., & Kubo, M. 2008, ApJ, 687, 658
Xu, Y., Cao, W., Jing, J., & Wang, H. 2012, ApJ, 750, L7
Xu, Y., Cao, W., Liu, C., et al. 2006, ApJ, 641, 1210
Xu, Y., Yang, G., Qiu, J., et al. 2004, ChJAA (Chin. J. Astron. Astrophys.), 4, 481
Zirin, H. 1988, Astrophysics of the Sun (Cambridge: Cambridge University Press)